Metabolic subtyping of pheochromocytoma and paraganglioma by 18F-FDG pharmacokinetics using dynamic PET/CT scanning

Berkel, A. van; Vriens, D.; Visser, E.P.; Janssen, M.J.R.; Gotthardt, M.; Hermus, A.R.M.M.; … ; Timmers, H.J.L.M.

Citation

Berkel, A. van, Vriens, D., Visser, E. P., Janssen, M. J. R., Gotthardt, M., Hermus, A. R. M. M., … Timmers, H. J. L. M. (2018). Metabolic subtyping of pheochromocytoma and paraganglioma by 18F-FDG pharmacokinetics using dynamic PET/CT scanning. *Journal Of Nuclear Medicine*, *60*(6), 745-751. doi:10.2967/jnumed.118.216796

Metabolic Subtyping of Pheochromocytoma and Paraganglioma by ^{18}F-FDG Pharmacokinetics Using Dynamic PET/CT Scanning

Anouk van Berkel[1], Dennis Vriens[2], Eric P. Visser[3], Marcel J.R. Janssen[3], Martin Gotthardt[3], Ad R.M.M. Hermus[1], Lioe-Fee de Geus-Oei[2,4], and Henri J.L.M. Timmers[1]

[1]Division of Endocrinology, Department of Internal Medicine, Radboud University Medical Center, Nijmegen, The Netherlands; [2]Department of Radiology, Leiden University Medical Center, Leiden, The Netherlands; [3]Department of Radiology and Nuclear Medicine, Radboud University Medical Center, Nijmegen, The Netherlands; and [4]MIRA Institute for Biomedical Technology and Technical Medicine, University of Twente, Enschede, The Netherlands

Static single–time-frame ^{18}F-FDG PET/CT is useful for the localization and functional characterization of pheochromocytomas and paragangliomas (PPGLs). ^{18}F-FDG uptake varies between PPGLs with different genotypes, and the highest SUVs are observed in cases of succinate dehydrogenase (*SDH*) mutations, possibly related to enhanced aerobic glycolysis in tumor cells. The exact determinants of ^{18}F-FDG accumulation in PPGLs are unknown. We performed dynamic PET/CT scanning to assess whether in vivo ^{18}F-FDG pharmacokinetics has added value over static PET to distinguish different genotypes. **Methods:** Dynamic ^{18}F-FDG PET/CT was performed on 13 sporadic PPGLs and 13 PPGLs from 11 patients with mutations in *SDH* complex subunits B and D, von Hippel-Lindau (*VHL*), *RET,* and neurofibromin 1 (*NF1*). Pharmacokinetic analysis was performed using a 2-tissue-compartment tracer kinetic model. The derived transfer rate-constants for transmembranous glucose flux (K_1 [in], k_2 [out]) and intracellular phosphorylation (k_3), along with the vascular blood fraction (V_b), were analyzed using nonlinear regression analysis. Glucose metabolic rate (MR_{glc}) was calculated using Patlak linear regression analysis. The SUV_{max} of the lesions was determined on additional static PET/CT images. **Results:** Both MR_{glc} and SUV_{max} were significantly higher for hereditary cluster 1 (*SDHx, VHL*) tumors than for hereditary cluster 2 (*RET, NF1*) and sporadic tumors ($P < 0.01$ and $P < 0.05$, respectively). Median k_3 was significantly higher for cluster 1 than for sporadic tumors ($P < 0.01$). Median V_b was significantly higher for cluster 1 than for cluster 2 tumors ($P < 0.01$). No statistically significant differences in K_1 and k_2 were found between the groups. Cutoffs for k_3 to distinguish between cluster 1 and other tumors were established at 0.015 min^{-1} (100% sensitivity, 15.8% specificity) and 0.636 min^{-1} (100% specificity, 85.7% sensitivity). MR_{glc} significantly correlated with SUV_{max} ($P = 0.001$) and k_3 ($P = 0.002$). **Conclusion:** In vivo metabolic tumor profiling in patients with PPGL can be achieved by assessing ^{18}F-FDG pharmacokinetics using dynamic PET/CT scanning. Cluster 1 PPGLs can be reliably identified by a high ^{18}F-FDG phosphorylation rate.

Key Words: pheochromocytoma; paraganglioma; succinate dehydrogenase; Warburg effect; ^{18}F-fluorodeoxyglucose positron emission tomography

J Nucl Med 2019; 60:745–751
DOI: 10.2967/jnumed.118.216796

Static ^{18}F-FDG PET/CT has been proven useful for localization and characterization of both primary and metastatic pheochromocytomas and paragangliomas (PPGLs) (*1*). These catecholamine-producing tumors derive from the adrenal medulla and extraadrenal sympathetic chromaffin tissues. At least one third of PPGLs are associated with hereditary cancer susceptibility syndromes (*2*). Germline mutations have been identified in more than 15 well-characterized genes, most commonly in succinate dehydrogenase (*SDH*) complex subunits B and D (*SDHB/D*), *RET,* von Hippel-Lindau (*VHL*), and neurofibromin 1 (*NF1*) (*2,3*). Furthermore, somatic mutations are found in at least one third of sporadic PPGLs (*2*). Hereditary PPGLs can be segregated into 2 clusters based on their transcription profiles: cluster 1 (*SDH, VHL*) is enriched for genes that are associated with the hypoxic response, and cluster 2 (*RET, NF1*) implicates gene mutations that activate kinase signaling (*4,5*). *SDHB* mutations are associated with a particularly malignant phenotype (*6–8*).

The degree of ^{18}F-FDG uptake mirrors glucose metabolism in tumor cells and varies between different PPGL genotypes. The highest SUVs on static PET/CT images are observed in *SDHx*- and *VHL*-related tumors (*9–11*). The high SUVs observed in cluster 1 PPGLs are currently not well explained or reflected by dedifferentiation or high proliferation rate (*9,12–14*). Increased glucose uptake could be due rather to genotype-related changes in energy metabolism (*15,16*). This possibility is supported by our previous observation that ^{18}F-FDG accumulation in *SDHx*-related PPGLs is associated with increased expression of hexokinases, indicating an increase in aerobic glycolysis, also known as the Warburg effect (*10*). Alternatively, high SUVs could be related to a high proportion of unmetabolized (e.g., unphosphorylated) ^{18}F-FDG present in the PPGL tissue. Dynamic ^{18}F-FDG PET/CT gives the opportunity to determine the proportion of unmetabolized (e.g., unphosphorylated) ^{18}F-FDG (*17*). The unmetabolized ^{18}F-FDG includes ^{18}F-FDG located in compartments such as

---

Received Jul. 3, 2018; revision accepted Oct. 29, 2018.

For correspondence or reprints contact: Anouk van Berkel, Radboud University Medical Center, Department of Internal Medicine, Division of Endocrinology 471, P.O. Box 9101, 6500 HB Nijmegen, The Netherlands.
E-mail: anouk.vanberkel@radboudumc.nl

the extracellular spaces (in the blood plasma, in the extravascular extracellular space) and the cells. Pharmacokinetic analysis of dynamic PET/CT allows quantitative assessment of in vivo glucose metabolic rate (MR_{glc}). Additionally, pharmacokinetic rate-constants of ^{18}F-FDG metabolism and V_b can be calculated using a 2-tissue-compartment model (*17*).

The aims of this study were, first, to assess in vivo ^{18}F-FDG uptake and pharmacokinetics across sporadic and hereditary PPGLs using dynamic multiple–time-frame PET/CT scanning to analyze the glycolytic activity of cluster 1 PPGLs and, second, to investigate whether dynamic PET/CT has added value over static ^{18}F-FDG PET/CT for distinguishing between different genotypes.

MATERIALS AND METHODS

Patients

Between October 2013 and April 2017, we prospectively included 26 patients who underwent ^{18}F-FDG PET/CT imaging as part of their diagnostic evaluation for PPGL. The initial 15 patients were included consecutively regardless of genotype. To achieve a representative mix of different hereditary cases, the additional 11 patients were selected for inclusion on the basis of (high pretest suspicion of) the presence of a germline mutation. All patients were investigated at the Radboud University Medical Center. Exclusion criteria were diabetes mellitus, a fasting glucose level of at least 8.0 mmol·L^{-1}, severe claustrophobia, breast feeding, and pregnancy. Twenty-four patients (13 men, 11 women; mean age, 52.7 y; range, 20–85 y) were analyzed, as 2 patients were excluded because of fasting hyperglycemia at the time of scanning and were later proven to have diabetes mellitus. The biochemical diagnosis of PPGL had been confirmed in all cases. In 20 patients, the diagnosis of PPGL was reconfirmed histologically after surgery. Twenty-one patients had nonmetastatic PPGLs (19 adrenal, 2 extraadrenal). Three patients had metastatic PPGLs, including one with retroaortic lymph node metastasis, one with retrocaval lymph node metastasis, and one with both paraaortic lymph node and thoracic spine bone metastasis. The presence of germline mutations and large deletions in *SDHA/B/C/D/AF2, VHL, RET, TMEM127,* and *MAX* was investigated using standard procedures. Eleven patients had an underlying mutation. The others were classified as having apparently sporadic disease. Patient characteristics are listed in Table 1. Plasma concentrations of free metanephrines were assayed using high-performance liquid chromatography (*18*). Biochemical phenotypes were categorized as described previously (*19*). Tumor sizes were recorded from pathology reports. The study was approved by the Institutional Review Board

TABLE 1
Patient Characteristics

Patient no.	Sex	Genotype	Age (y)	Tumor location	Status	Maximum tumor diameter (cm)	Biochemical phenotype
1	M	NF1	66	LA	Primary	1.2	E + NE
2	F	NF1	31	LA	Primary	4.0	E + NE
3	F	RET	62	LA	Primary	3.4	E + NE
4	F	RET	20	RA	Primary	3.5	E + NE
5	M	RET	35	RA	Primary	2.1	E + NE
6	M	RET	70	LA	Primary	3.0	E
7	F	SDHA	63	LA	Primary	NA	NE + DA
				EA (thoracic spine)	Metastatic	NA	NE + DA
				EA (paraaortic lymph node)	Metastatic	NA	NE + DA
8	M	SDHA	35	EA (retroaortic lymph node)	Metastatic	NA	DA
9	M	SDHB	46	EA (dorsolateral bladder)	Recurrent	NA	NE + DA
10	M	SDHD	64	RA	Primary	1.5	NE + DA
11	M	VHL	48	RA	Primary	2.2	NE
12	F	Sporadic	55	LA	Primary	11.0	E + NE
13	F	Sporadic	34	RA	Primary	5.0	E + NE
14	M	Sporadic	51	EA (retrocaval lymph node)	Metastatic	2.0	NE
15	F	Sporadic	33	LA	Primary	4.0	E + NE
16	F	Sporadic	56	EA (paraaortic lymph node)	Primary	1.4	NE
17	M	Sporadic	66	LA	Primary	1.8	E
18	M	Sporadic	85	RA	Primary	NA	NE
19	M	Sporadic	55	LA	Primary	3.5	E + NE
20	M	Sporadic	43	LA	Primary	10.0	E + NE
21	F	Sporadic	73	LA	Primary	12.5	NE + DA
22	F	Sporadic	55	RA	Primary	1.5	E
23	M	Sporadic	64	RA	Primary	5.0	E + NE
24	F	Sporadic	55	LA	Primary	6.0	E + NE

LA = left adrenal; RA = right adrenal; EA = extraadrenal; NA = not available; E = epinephrine; NE = norepinephrine; DA = dopamine.

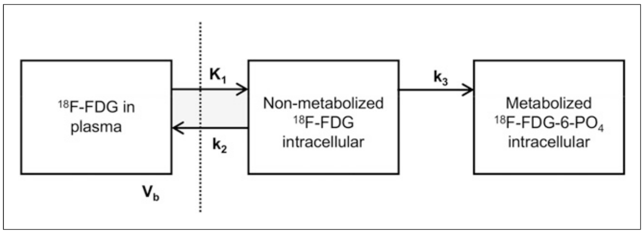

FIGURE 1. Irreversible 2-tissue-compartment model for ^{18}F-FDG metabolism. Measured PET signal is combination of intracellular activity concentration of free ^{18}F-FDG (nonmetabolized ^{18}F-FDG in tissue), intracellular activity concentration of ^{18}F-FDG-6-phosphate (metabolized ^{18}F-FDG-6-PO$_4$ in tissue), and fraction of activity concentration of ^{18}F-FDG in blood plasma (V_b). By using dynamic PET/CT, pharmacokinetic rate-constants K_1 and k_2 (rate constants of transport of ^{18}F-FDG into and out of tumor cell by glucose transporters, in mL/g/min), k_3 (rate constant of cytoplasmic phosphorylation of ^{18}F-FDG by hexokinase, per minute), and V_b (in milliliters of blood per milliliter of tumor) can be determined using nonlinear least-squares regression of dynamic PET/CT data. Vertical dashed line represents cell membrane

of the Radboud University Medical Center, and written informed consent was obtained from each patient.

^{18}F-FDG PET/CT Image Acquisition and Reconstruction

Patients fasted for at least 6 h before scanning. Venous blood glucose levels were measured before ^{18}F-FDG infusion. All PET/CT scans were acquired on a Biograph mCT-40 (Siemens Medical Solutions), which was calibrated and harmonized and was certified by the European Association of Nuclear Medicine Research Ltd. in accordance with its guidelines (*20*). CT findings were used to select the index tumor lesion. After low-dose breath-hold spiral CT had been performed, free-breathing PET/CT images at a single bed position were acquired immediately after ^{18}F-FDG infusion in list mode for 55 min, with the patient supine and the index tumor centrally located in the field of view. Subsequently, static ^{18}F-FDG PET/CT from skull base to mid thigh was performed 66 ± 4 min (mean ± SD) after ^{18}F-FDG infusion for clinical purposes. A dose of 1.82 ± 0.23 MBq·kg^{-1} of ^{18}F-FDG (administered dose range, 83–202 MBq) was directly administered in an antecubital vein using a standardized injection protocol (8.0 mL at 0.2 mL·s^{-1}) with a remote-controlled pump, followed by a saline flush (40 mL at 8.0 mL·s^{-1}), after the start of acquisition. Data were acquired and reconstructed as previously described (*10,21*).

Image Analysis of Dynamic PET

Decay-corrected PET/CT images were reviewed using Inveon Research Workplace (version 4.2; Siemens Healthcare). Images were analyzed by one investigator under the supervision of two experienced nuclear medicine physicians.

Parametric images of MR$_{glc}$ were derived from tissue and plasma blood time–activity concentration curves using the Patlak linearization approach, with data acquired between 15 and 55 min after injection, as previously described (*17,22*). A detailed description of the Patlak graphical analyses and its assumptions has been published elsewhere (*23*).

Tracer pharmacokinetics were assessed by performing pharmacokinetic analysis on the basis of tissue and plasma blood time–activity concentration curves. The rate constants (K_1–k_3) and vascular blood fraction (V_b) were calculated using nonlinear least-squares regression analysis by assuming an irreversible 2-tissue-compartment model (Fig. 1). The optimization consisted of 99 random starting points with reproducible results to prevent the optimization algorithm from quitting when converging to a local minimum instead of the global minimum.

Image Analysis of Static PET

Static ^{18}F-FDG PET/CT scans were also evaluated semiquantitatively by SUV analysis. SUV$_{max}$ normalized for body weight was calculated as SUV = A/(IA × BW), where A is the activity concentration within the volume of interest (Bq·mL^{-1}), BW is body weight (g), and IA is injected activity (Bq). All calculated SUVs were decay-corrected using the half-life of ^{18}F.

Statistical Analysis

Parameter values strongly deviated from a (log)normal distribution and are therefore presented as median and range. For comparisons of MR$_{glc}$, SUV$_{max}$, pharmacokinetic rate-constants (K_1–k_3), and V_b across different genotypes, data were analyzed using the independent-samples Kruskal–Wallis test with the Dunn post hoc test. To test for differences between primary and metastatic PPGLs, the Mann–Whitney *U* test was used. Correlations were examined using the Spearman rank correlation test and presented as the fraction of the total variance explained (R^2). Cutoffs for mutations in cluster 1 (*SDHx, VHL*) were determined using receiver-operating-characteristic curve analysis, and the area under the curve was calculated. Statistical analysis was conducted using SPSS 20 (SPSS Inc.) and Prism 6 software (GraphPad Inc.). A 2-sided *P* value of less than 0.05 was considered to be statistically significant.

RESULTS

The results of semiquantitative and quantitative PET/CT analyses are summarized in Table 2. Dynamic ^{18}F-FDG PET/CT was directed at a single index tumor in the field of view of 1 bed position, except for patient 7, who had multiple lesions in the field of view. For this patient with metastatic disease, only the best-evaluable lesion was included in the data analysis, that is, a lymph node metastasis without necrosis or previous local treatment (^{131}I-metaiodobenzylguanidine therapy and external radiotherapy).

TABLE 2
^{18}F-FDG PET/CT Parameters

Parameter	All tumor lesions (n = 26)	Primary tumors (n = 22)	Metastases (n = 4)
MR$_{glc}$ (nmol·mL^{-1}·min^{-1})	53.6 (13.2–412.4)	49.4 (13.2–412.4)	137.6 (14.6–219.8)
SUV$_{max}$ (g·cm^{-3})	4.7 (1.3–21.1)	4.6 (1.3–19.6)	7.1 (2.0–21.1)
K_1 (mL·g^{-1}·min^{-1})	0.42 (0.10–3.25)	0.41 (0.18–3.25)	0.46 (0.96–0.51)
k_2 (min^{-1})	0.95 (0.13–2.82)	0.93 (0.13–2.83)	1.04 (0.24–1.15)
k_3 (min^{-1})	0.032 (0.011–0.170)	0.032 (0.014–0.151)	0.049 (0.011–0.170)
V_b (mL·mL^{-1})	0.148 (0.037–0.738)	0.144 (0.037–0.738)	0.182 (0.080–0.390)

Data are median followed by range in parentheses. No significant differences were observed between 2 groups (Mann–Whitney *U* test).

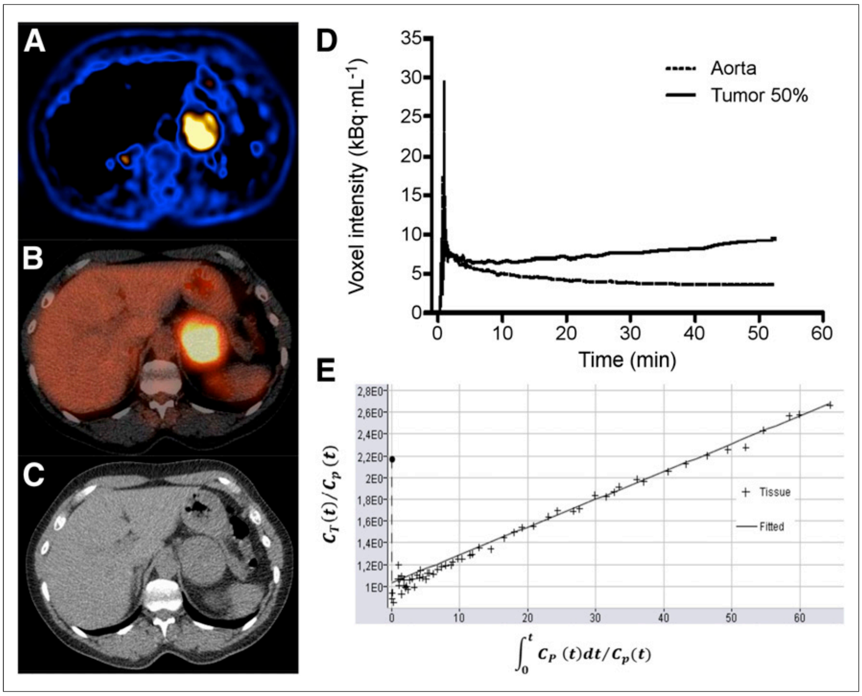

FIGURE 2. Dynamic ^{18}F-FDG PET/CT results in patient 24, with primary sporadic PPGL in left adrenal. (A) Parametric image of MR_{glc} from dynamic ^{18}F-FDG PET scan. (B) Static ^{18}F-FDG PET/CT scan. (C) CT scan. (D) Image-derived input function and tumor time–activity curve. (E) Patlak plot. Slope of Patlak plot equals influx constant K_i

Dynamic ^{18}F-FDG PET/CT in PPGLs

An example of a parametric image of MR_{glc} is shown in Figure 2. The median MR_{glc} for hereditary cluster 1 tumors (*SDHx, VHL*) was higher than that for hereditary cluster 2 tumors (*RET, NF1*) ($P < 0.01$) and apparently sporadic tumors ($P < 0.01$) (Fig. 3A).

Pharmacokinetic rate-constants in PPGLs across hereditary and apparently sporadic tumors are shown in Table 3 and Figure 4. The median k_3 for hereditary cluster 1 tumors (*SDHx, VHL*) was higher than that for apparently sporadic tumors ($P < 0.01$). The median V_b for hereditary cluster 1 tumors (*SDHx, VHL*) was higher than that for hereditary cluster 2 tumors (*RET, NF1*) ($P < 0.01$). V_b appeared to be independent of tumor location and size. To exclude bias toward metastatic lesions, and thereby toward genotype, a subanalysis was performed on primary lesions only, yielding similar results (Supplemental Table 1; supplemental materials are available at http://jnm.snmjournals.org).

Static Versus Dynamic ^{18}F-FDG PET/CT Across Genotypes

The median SUV_{max} for hereditary cluster 1 tumors (*SDHx, VHL*) was higher than that for hereditary cluster 2 tumors (*RET, NF1*) ($P < 0.01$) and apparently sporadic tumors ($P < 0.05$) (Fig. 3B).

Receiver-operating-characteristic curves were determined for the k_3 and SUV_{max} of all cluster 1 tumors ($n = 7$) and other (both cluster 2 and apparently sporadic, $n = 19$) tumors. The area under the curve was 0.880 for k_3 (95% confidence interval, 0.66–1.00; Fig. 5) and 0.910 for SUV_{max} (95% confidence interval, 0.80–1.00; Fig. 5). To provide 100% sensitivity, the upper reference to distinguish cluster 1 tumors from other tumors was established at 0.071 min^{-1} for k_3 (the minimum value for cluster 1 tumors), resulting in a specificity of 100%. To provide 100% sensitivity, the lower reference to distinguish cluster 1 tumors from other tumors was established at 4.7 for $SUV_{max,}$ resulting in a specificity of 68.4%, which is lower than for k_3.

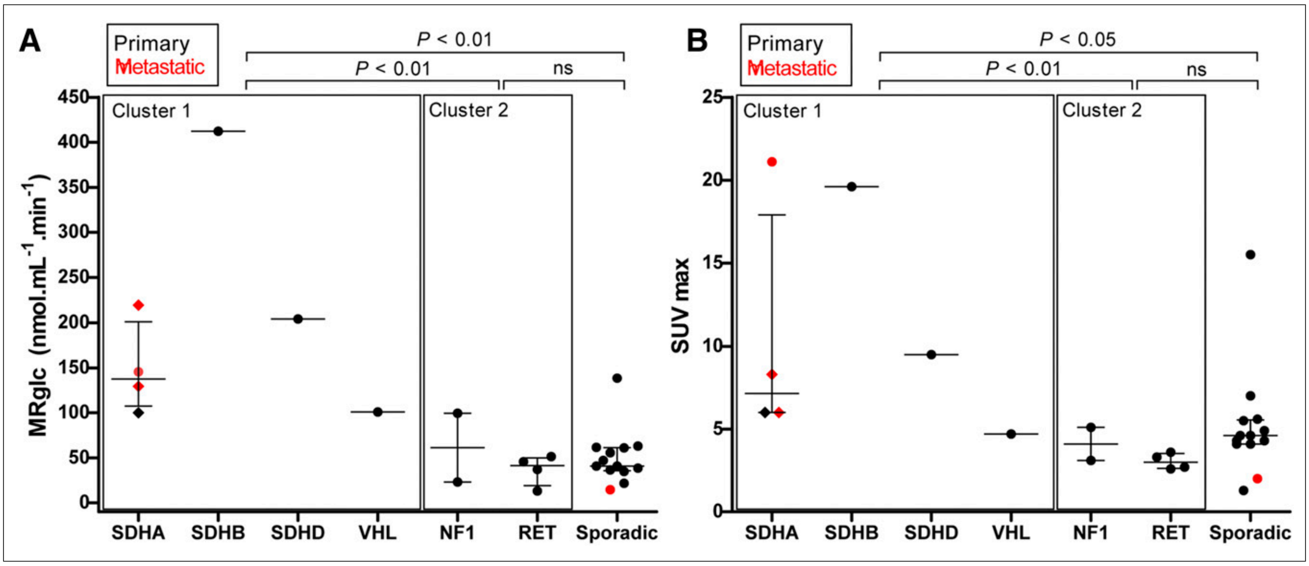

FIGURE 3. Scatterplots showing MR_{glc} (A) and ^{18}F-FDG SUV_{max} (B) in PPGLs across different genotypes. Horizontal bar represents median and interquartile range. Diamonds represent 3 different tumor locations in same patient (patient 7, Table 1). All SUVs are normalized for body weight and decay. *P* values are from Kruskal–Wallis with Dunn post hoc testing, and groups are compared as indicated. ns = not significant.

TABLE 3

^{18}F-FDG Pharmacokinetic Rate-Constants for Primary and Metastatic PPGLs

Rate constant	Hereditary cluster 1 tumors (*SDHx, VHL*) (n = 7)	Hereditary cluster 2 tumors (*RET, NF1*) (n = 6)	Sporadic tumors (n = 13)
K_1 (mL·g^{-1}·min^{-1})	0.28 (0.10–3.25)	0.44 (0.23–0.65)	0.50 (0.18–1.01)
k_2 (min^{-1})	0.79 (0.13–2.82)	1.08 (0.54–1.50)	0.99 (0.47–1.49)
k_3 (min^{-1})	0.084 (0.015–0.170)*	0.041 (0.015–0.062)	0.025 (0.011–0.059)
V_b (mL·mL^{-1})	0.219 (0.080–0.738)†	0.105 (0.037–0.128)	0.151 (0.072–0.300)

*Significantly higher than sporadic tumor values ($P < 0.01$, Kruskal–Wallis with post hoc Dunn test).

†Significantly higher than hereditary cluster 2 values ($P < 0.01$, Kruskal–Wallis with post hoc Dunn test).

Data are median followed by range in parentheses.

Determinants of ^{18}F-FDG Uptake in PPGLs

The correlation coefficients between MR_{glc} and calculated SUVs and pharmacokinetic rate-constants are summarized in Table 4. MR_{glc} significantly correlated with SUV_{max} (R^2 = 0.475; 95% confidence interval, 0.291–0.882; P = 0.001) and k_3 (R^2 = 0.358; 95% confidence interval, 0.181–0.832; P = 0.002) (Supplemental Fig. 1). No correlations were found between MR_{glc} and K_1, k_2, or V_b.

DISCUSSION

Our study provides the first quantitative assessment of in vivo MR_{glc} in PPGLs across some genotypes, using dynamic ^{18}F-FDG PET/CT scanning. We found profound genotype-specific differences in ^{18}F-FDG pharmacokinetics between cluster 1 (*SDHx, VHL*) and cluster 2 (*RET, NF1*) or sporadic PPGLs. Both MR_{glc} and SUV_{max} were significantly higher in cluster 1 PPGLs than in cluster 2 and sporadic tumors. Moreover, the glucose phosphorylation rate-constant k_3 was significantly higher in cluster 1 tumors than in sporadic tumors, and the V_b was significantly higher in cluster 1 than in cluster 2. Furthermore, we demonstrated that k_3 can be used to reliably distinguish between cluster 1 and other tumors.

PPGLs are usually benign, but up to 15%–20% develop into metastatic disease. Currently, there are no reliable histologic or molecular markers for malignancy. The strongest predictor for the development of metastases is the presence of a germline *SDHB* mutation (*24*). In addition, the prognosis is poorest in patients with metastatic PPGL due to an underlying *SDHB* mutation (*8*). Therefore, early identification of PPGLs of an aggressive or *SDHB*-related nature is key for proper management. Radionuclide imaging is instrumental for tumor localization but also for functional characterization of PPGLs (*25*).

We have previously shown that PPGL features on ^{18}F-FDG PET/CT can point toward particular hereditary syndromes and can be used, along with other clinical characteristics, to guide the genetic testing (*9,10,26*). Using static ^{18}F-FDG PET/CT, we have observed prominent ^{18}F-FDG accumulation in *SDHx* and *VHL* PPGLs, exhibiting higher SUVs than other tumors. This finding is probably related to the fact that cluster 1 mutations result in an HIF-driven activation of the hypoxic–angiogenic pathway and metabolic shift toward aerobic glycolysis, known as the Warburg effect (*16,27,28*). However, ^{18}F-FDG accumulation is influenced by many factors, such as the presence of necrosis, vascular density, activity of glucose transporters, and glycolytic enzymes (hexokinases). Therefore, the exact determinants of ^{18}F-FDG uptake in PPGLs remains to be established.

Quantitative dynamic ^{18}F-FDG PET/CT is considered the gold standard for measuring in vivo tumor glucose metabolism. MR_{glc} provides the most accurate estimate of glucose consumption (*29,30*). The cellular expression and activity of hexokinases are best reflected by the pharmacokinetic rate-constant k_3. The major hexokinase isoform, hexokinase-2, is regulated by HIF-1α and predominantly

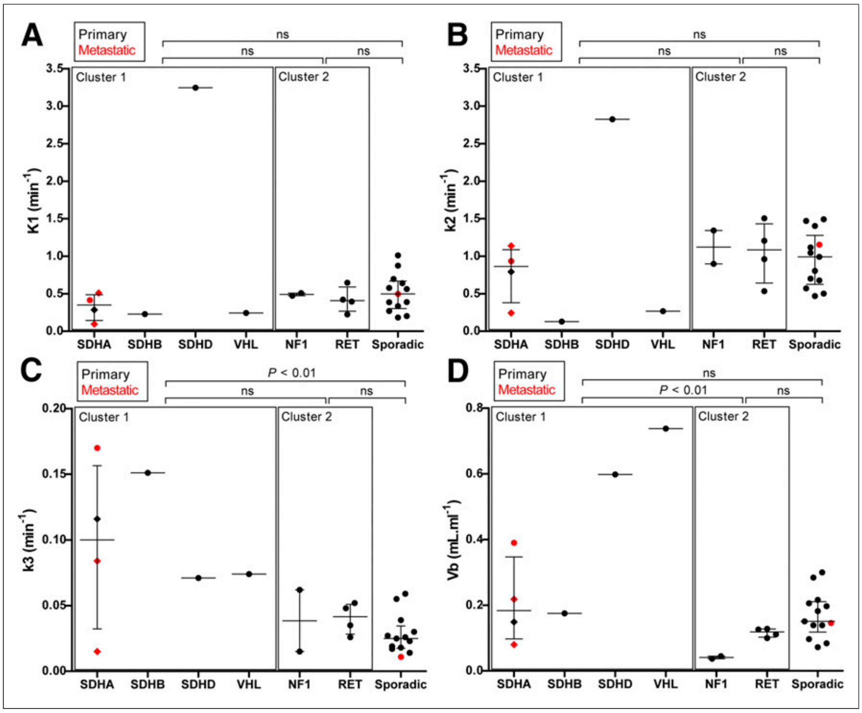

FIGURE 4. Pharmacokinetic rate-constants (K_1, k_2, and k_3) and blood volume fraction (V_b) in PPGLs across different genotypes. Horizontal bar represents median and interquartile range (IQR). Diamonds represent 3 different tumor locations in same patient (patient 7). P values are from Kruskal–Wallis with Dunn post hoc testing, and groups are compared as indicated. ns = not significant.

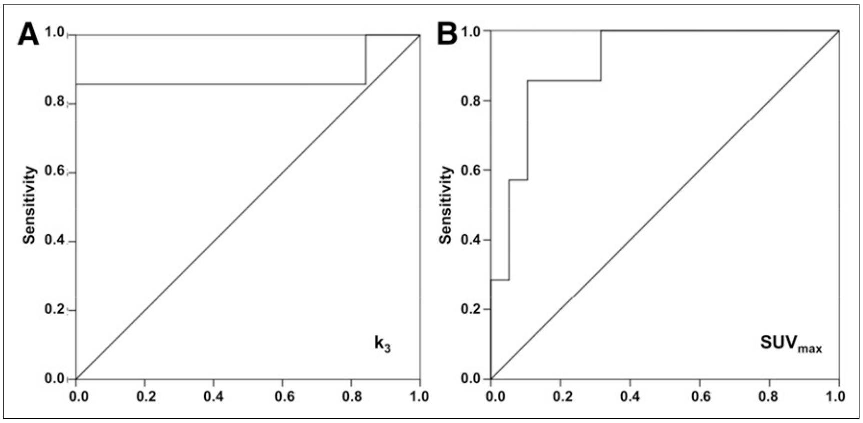

FIGURE 5. Receiver-operating-characteristic curve for pharmacokinetic rate-constant k_3 (A) and $\mathrm{SUV}_{\max}$ (B). This curve was constructed from k_3 and $\mathrm{SUV}_{\max}$ of cluster 1 tumors vs. other (cluster 2 and sporadic) tumors in patients with PPGL. Diagonal line represents line of no discrimination.

expressed in tumor cells that exhibit the Warburg effect (*16,31*). Okazumi et al. (*32*) found a significant correlation between k_3 and hexokinase activity in liver tumors. Strauss et al. (*33*) demonstrated that K_1 and k_3 reflect gene activity of glucose transporters and hexokinases, respectively, and are correlated with their cellular expression. They also reported an association between k_3 and HIF-1α (*34*). In the current study, we found increased k_3 values in cluster 1 PPGLs, as well as a significant correlation between k_3, $\mathrm{MR}_{\mathrm{glc}}$, and SUV, suggesting that increased accumulation of ^{18}F-FDG is determined largely by increased hexokinase activity. In contrast, K_1–k_2 values did not differ between clusters, suggesting that glucose transporter activity does not account for genotype-specific differences in ^{18}F-FDG avidity.

Differences in ^{18}F-FDG uptake could also reflect differences in tumor blood flow and, in parallel, the delivery and metabolism of ^{18}F-FDG. The dynamic PET-derived parameter $\mathrm{V_b}$ represents the fraction of blood within the tumor lesion. We observed relatively high average $\mathrm{V_b}$ values in PPGL when compared with other types of tumors (*34–36*), but also a large variability between PPGLs. Favier et al. have shown that PPGLs are hypervascular tumors with highly heterogeneous vascular patterns (*37*). This is probably related to the genotype-specific impact on angiogenesis. They also found HIF-induced overexpression of vascular endothelial growth factor in *SDHx* and *VHL*-related PPGLs (*16*). We also demonstrated that vascular endothelial growth factor expression and endothelial surface area was higher in *SDHx*-related PPGLs than in cluster 2 and sporadic tumors (*10*). In line with this theory, we observed that $\mathrm{V_b}$ was significantly higher in cluster 1 than cluster 2 PPGLs and significantly correlated with $\mathrm{SUV}_{\max}$. Therefore, besides increased glycolysis, increased vascularity or blood perfusion may be largely responsible for the higher $\mathrm{SUV}_{\max}$ in cluster 1 tumors.

TABLE 4
Determinants of $\mathrm{MR}_{\mathrm{glc}}$

Parameter	$\mathrm{MR}_{\mathrm{glc}}$ (nmol·mL^{-1}·min^{-1}) R^2 (95% CI)	*P*
$\mathrm{SUV}_{\max}$	0.475 (0.291 to 0.882)	0.001*
K_1 (mL·g^{-1}·min^{-1})	0.066 (−0.629 to 0.156)	0.228
k_2 (min^{-1})	0.145 (−0.732 to 0.073)	0.067
k_3 (min^{-1})	0.358 (0.181 to 0.832)	0.002*
$\mathrm{V_b}$ (mL·mL^{-1})	0.107 (−0.103 to 0.677)	0.118

---

*$P < 0.01$.
CI = confidence interval.

Recently, Barbolosi et al. calculated the proportions of unmetabolized and metabolized ^{18}F-FDG and kinetic parameters in a small number of sporadic primary PPGLs as compared with other tumors (*36*). Their model was based on a new mathematic approach that integrates a measurement error model without the acquisition of dynamic images. Interestingly, they found that as compared with other tumors, PPGLs were characterized by a relatively low glycolytic activity as expressed by a high proportion of unmetabolized ^{18}F-FDG and relatively low k_3 value. Furthermore, K_i (net influx rate constant) and $\mathrm{V_b}$ were relatively higher. In contrast to our current study, however, no comparisons were made between PPGLs of different genotypes. Nevertheless, we indeed also observed relatively low k_3 values when compared with previous measurements of k_3 in other tumors by our group (*35*). These results confirm that the glycolytic effect due to the Warburg effect might be less pronounced than in several other types of cancer. Besides a switch to glycolysis, increased uptake of ^{18}F-FDG could also be affected directly by the accumulation and paracrine effects of the oncometabolite succinate, as was recently suggested by a recent study by Garrigue et al. (*38*). They demonstrated that exposure to succinate increased the in vivo ^{18}F-FDG uptake in an adenocarcinoma xenograft mouse model. Additional in vitro studies showed that succinate did not affect ^{18}F-FDG uptake by tumors cells per se but rather by endothelial cells. These results suggest the presence of a metabolic crosstalk between tumor cells and the microenvironment. The latter phenomenon has been previously described in PPGL by others (*39*). Unfortunately, our present study cannot further elucidate these mechanisms, since dynamic ^{18}F-FDG PET cannot distinguish the metabolized and unmetabolized component of ^{18}F-FDG in tumor cells versus stromal cells.

Although, on average, we found a significantly higher $\mathrm{MR}_{\mathrm{glc}}$ and $\mathrm{SUV}_{\max}$ in cluster 1 PPGLs, individual values for both parameters considerably overlapped between cluster 1 and sporadic tumors. From a clinical point of view, it would be useful to identify the genotypes on the basis of functional imaging in individual patients, especially high-risk *SDHB* tumors. This step could be particularly useful in patients carrying variants of unknown significance. Our results suggest that dynamic ^{18}F-FDG PET/CT could serve this purpose when hexokinase activity (k_3) is considered. We acknowledge that this study is limited by the small sample size. Obviously, our results would need replication in a larger study sample that includes a better variety of genotypes, primary PPGLs in various locations, and metastases. Such a study would also permit analysis of within-cluster variability, such as *SDHx* versus *VHL*. In addition, there are some practical constraints to the clinical application of somewhat laborious dynamic PET in clinical practice. These, however, could be overcome by simplification of the protocol, such as in the Hunter method that was mentioned previously (*36*). Also, proton (^{1}H) nuclear MR spectroscopy was shown to discriminate between *SDH* and non-*SDH* tumors by looking at the presence or absence of a succinate peak, respectively (*40,41*). This imaging technique could be complementary to dynamic PET/CT for in vivo metabolic profiling.

CONCLUSION

In vivo metabolic tumor profiling in patients with PPGL by assessing ^{18}F-FDG pharmacokinetics can be better achieved using dynamic PET/CT than using static PET/CT. With this technique, cluster 1 PPGLs can reliably be identified by a high ^{18}F-FDG phosphorylation rate.

DISCLOSURE

This research was supported by the European Union Seventh Framework Programme (FP7/2007-2013) under grant agreement 259735 (ENSAT CANCER). No other potential conflict of interest relevant to this article was reported.

ACKNOWLEDGMENTS

We thank the PET/CT technologists from the Radboud University Medical Center for assistance with the dynamic PET/CT scans.

REFERENCES

1. Castinetti F, Kroiss A, Kumar R, Pacak K, Taieb D. 15 years of paraganglioma: imaging and imaging-based treatment of pheochromocytoma and paraganglioma. *Endocr Relat Cancer.* 2015;22:T135–T145.
2. Fishbein L, Leshchiner I, Walter V, et al. Comprehensive molecular characterization of pheochromocytoma and paraganglioma. *Cancer Cell.* 2017;31:181–193.
3. Favier J, Amar L, Gimenez-Roqueplo AP. Paraganglioma and phaeochromocytoma: from genetics to personalized medicine. *Nat Rev Endocrinol.* 2015;11:101–111.
4. Eisenhofer G, Huynh TT, Pacak K, et al. Distinct gene expression profiles in norepinephrine- and epinephrine-producing hereditary and sporadic pheochromocytomas: activation of hypoxia-driven angiogenic pathways in von Hippel-Lindau syndrome. *Endocr Relat Cancer.* 2004;11:897–911.
5. López-Jiménez E, Gomez-Lopez G, Leandro-Garcia LJ, et al. Research resource: transcriptional profiling reveals different pseudohypoxic signatures in SDHB and VHL-related pheochromocytomas. *Mol Endocrinol.* 2010;24:2382–2391.
6. Timmers HJ, Kozupa A, Eisenhofer G, et al. Clinical presentations, biochemical phenotypes, and genotype-phenotype correlations in patients with succinate dehydrogenase subunit B-associated pheochromocytomas and paragangliomas. *J Clin Endocrinol Metab.* 2007;92:779–786.
7. Neumann HP, Pawlu C, Peczkowska M, et al. Distinct clinical features of paraganglioma syndromes associated with SDHB and SDHD gene mutations. *JAMA.* 2004;292:943–951.
8. Amar L, Baudin E, Burnichon N, et al. Succinate dehydrogenase B gene mutations predict survival in patients with malignant pheochromocytomas or paragangliomas. *J Clin Endocrinol Metab.* 2007;92:3822–3828.
9. Timmers HJ, Chen CC, Carrasquillo JA, et al. Staging and functional characterization of pheochromocytoma and paraganglioma by ^{18}F-fluorodeoxyglucose (^{18}F-FDG) positron emission tomography. *J Natl Cancer Inst.* 2012;104:700–708.
10. van Berkel A, Rao JU, Kusters B, et al. Correlation between in vivo ^{18}F-FDG PET and immunohistochemical markers of glucose uptake and metabolism in pheochromocytoma and paraganglioma. *J Nucl Med.* 2014;55:1253–1259.
11. Timmers HJ, Kozupa A, Chen CC, et al. Superiority of fluorodeoxyglucose positron emission tomography to other functional imaging techniques in the evaluation of metastatic SDHB-associated pheochromocytoma and paraganglioma. *J Clin Oncol.* 2007;25:2262–2269.
12. Timmers HJ, Chen CC, Carrasquillo JA, et al. Comparison of ^{18}F-fluoro-L-DOPA, ^{18}F-fluoro-deoxyglucose, and ^{18}F-fluorodopamine PET and ^{123}I-MIBG scintigraphy in the localization of pheochromocytoma and paraganglioma. *J Clin Endocrinol Metab.* 2009;94:4757–4767.
13. Taïeb D, Sebag F, Barlier A, et al. ^{18}F-FDG avidity of pheochromocytomas and paragangliomas: a new molecular imaging signature? *J Nucl Med.* 2009;50:711–717.
14. Venkatesan AM, Trivedi H, Adams KT, Kebebew E, Pacak K, Hughes MS. Comparison of clinical and imaging features in succinate dehydrogenase-positive versus sporadic paragangliomas. *Surgery.* 2011;150:1186–1193.
15. Jochmanová I, Yang C, Zhuang Z, Pacak K. Hypoxia-inducible factor signaling in pheochromocytoma: turning the rudder in the right direction. *J Natl Cancer Inst.* 2013;105:1270–1283.
16. Favier J, Briere JJ, Burnichon N, et al. The Warburg effect is genetically determined in inherited pheochromocytomas. *PLoS One.* 2009;4:e7094.
17. Vriens D, Visser EP, de Geus-Oei LF, Oyen WJ. Methodological considerations in quantification of oncological FDG PET studies. *Eur J Nucl Med Mol Imaging.* 2010;37:1408–1425.
18. Lenders JW, Eisenhofer G, Armando I, Keiser HR, Goldstein DS, Kopin IJ. Determination of metanephrines in plasma by liquid chromatography with electrochemical detection. *Clin Chem.* 1993;39:97–103.
19. Eisenhofer G, Pacak K, Huynh TT, et al. Catecholamine metabolomic and secretory phenotypes in phaeochromocytoma. *Endocr Relat Cancer.* 2010;18:97–111.
20. Boellaard R, O'Doherty MJ, Weber WA, et al. FDG PET and PET/CT: EANM procedure guidelines for tumour PET imaging: version 1.0. *Eur J Nucl Med Mol Imaging.* 2010;37:181–200.
21. Meijer TW, de Geus-Oei LF, Visser EP, et al. Tumor delineation and quantitative assessment of glucose metabolic rate within histologic subtypes of non-small cell lung cancer by using dynamic ^{18}F fluorodeoxyglucose PET. *Radiology.* 2017;283:547–559.
22. de Geus-Oei LF, Visser EP, Krabbe PF, et al. Comparison of image-derived and arterial input functions for estimating the rate of glucose metabolism in therapy-monitoring ^{18}F-FDG PET studies. *J Nucl Med.* 2006;47:945–949.
23. Patlak CS, Blasberg RG, Fenstermacher JD. Graphical evaluation of blood-to-brain transfer constants from multiple-time uptake data. *J Cereb Blood Flow Metab.* 1983;3:1–7.
24. Eisenhofer G, Goldstein DS, Sullivan P, et al. Biochemical and clinical manifestations of dopamine-producing paragangliomas: utility of plasma methoxytyramine. *J Clin Endocrinol Metab.* 2005;90:2068–2075.
25. Taïeb D, Timmers HJ, Shulkin BL, Pacak K. Renaissance of ^{18}F-FDG positron emission tomography in the imaging of pheochromocytoma/paraganglioma. *J Clin Endocrinol Metab.* 2014;99:2337–2339.
26. Gimenez-Roqueplo AP, Lehnert H, Mannelli M, et al. Phaeochromocytoma, new genes and screening strategies. *Clin Endocrinol (Oxf).* 2006;65:699–705.
27. Selak MA, Armour SM, MacKenzie ED, et al. Succinate links TCA cycle dysfunction to oncogenesis by inhibiting HIF-alpha prolyl hydroxylase. *Cancer Cell.* 2005;7:77–85.
28. Dahia PL; Familial Pheochromocytoma Consortium. Transcription association of VHL and SDH mutations link hypoxia and oxidoreductase signals in pheochromocytomas. *Ann N Y Acad Sci.* 2006;1073:208–220.
29. Basu S, Zaidi H, Alavi A. Clinical and research applications of quantitative PET imaging. *PET Clin.* 2007;2:161–172.
30. Dimitrakopoulou-Strauss A, Pan L, Strauss LG. Quantitative approaches of dynamic FDG-PET and PET/CT studies (dPET/CT) for the evaluation of oncological patients. *Cancer Imaging.* 2012;12:283–289.
31. Mathupala SP, Ko YH, Pedersen PL. Hexokinase-2 bound to mitochondria: cancer's Stygian link to the "Warburg effect" and a pivotal target for effective therapy. *Semin Cancer Biol.* 2009;19:17–24.
32. Okazumi S, Enomoto K, Ozaki M, et al. Evaluation of the effect of treatment in patients with liver tumors using ^{18}F-fluorodeoxyglucose PET [in Japanese]. *Kaku Igaku.* 1989;26:793–797.
33. Strauss LG, Koczan D, Klippel S, et al. Dynamic PET with ^{18}F-deoxyglucose (FDG) and quantitative assessment with a two-tissue compartment model reflect the activity of glucose transporters and hexokinases in patients with colorectal tumors. *Am J Nucl Med Mol Imaging.* 2013;3:417–424.
34. Strauss LG, Dimitrakopoulou-Strauss A, Koczan D, et al. ^{18}F-FDG kinetics and gene expression in giant cell tumors. *J Nucl Med.* 2004;45:1528–1535.
35. Vriens D, Disselhorst JA, Oyen WJ, de Geus-Oei LF, Visser EP. Quantitative assessment of heterogeneity in tumor metabolism using FDG-PET. *Int J Radiat Oncol Biol Phys.* 2012;82:e725–e731.
36. Barbolosi D, Hapdey S, Battini S, et al. Determination of the unmetabolised ^{18}F-FDG fraction by using an extension of simplified kinetic analysis method: clinical evaluation in paragangliomas. *Med Biol Eng Comput.* 2016;54:103–111.
37. Favier J, Plouin PF, Corvol P, Gasc JM. Angiogenesis and vascular architecture in pheochromocytomas: distinctive traits in malignant tumors. *Am J Pathol.* 2002;161:1235–1246.
38. Garrigue P, Bodin-Hullin A, Balasse L, et al. The evolving role of succinate in tumor metabolism: an ^{18}F-FDG-based study. *J Nucl Med.* 2017;58:1749–1755.
39. Rapizzi E, Fucci R, Giannoni E, et al. Role of microenvironment on neuroblastoma SK-N-AS SDHB-silenced cell metabolism and function. *Endocr Relat Cancer.* 2015;22:409–417.
40. Lussey-Lepoutre C, Bellucci A, Morin A, et al. In vivo detection of succinate by magnetic resonance spectroscopy as a hallmark of SDHx mutations in paraganglioma. *Clin Cancer Res.* 2016;22:1120–1129.
41. Varoquaux A, le Fur Y, Imperiale A, et al. Magnetic resonance spectroscopy of paragangliomas: new insights into in vivo metabolomics. *Endocr Relat Cancer.* 2015;22:M1–M8.